

1 On the properties of a negative-ion TPC prototype
2 with GridPix readout

3 C. Ligtenberg^{a,*}, M. van Beuzekom^a, Y. Bilevych^b, K. Desch^b,
4 H. van der Graaf^a, F. Hartjes^a, K. Heijhoff^{a,b}, J. Kaminski^b, P.M. Kluit^a,
5 N. van der Kolk^a, G. Raven^a, J. Timmermans^a

6 ^a*Nikhef, Science Park 105, 1098 XG Amsterdam, The Netherlands*

7 ^b*Physikalisches Institut, University of Bonn, Nussallee 12, 53115 Bonn,*
8 *Germany*

9 **Abstract**

10 The performance of a GridPix detector to read out a negative ion TPC was stud-
11 ied using a module with four GridPix chips that are based on the Timepix3 pixe-
12 lated readout ASIC. The quad module dimensions are 39.6 mm × 28.38 mm, and
13 the maximum drift distance is 40 mm. The TPC is operated using a 93.6/5.0/1.4
14 gas mixture (by volume) of Ar/iC₄H₁₀/CS₂ with a small amount of oxygen and
15 water vapour at a pressure of 1030 mbar and a temperature of 297 K. Tracks
16 were produced by a pulsed N₂ laser. The GridPix chips are sensitive to single
17 drift ions, and allow for the determination of the drift distance using the veloc-
18 ities of the different ion species. The 1.56 ns time resolution of the Timepix3
19 chips allows for a precise determination of the drift properties in the longi-
20 tudinal direction. The measured mobility of majority ion charge carriers is
21 $(1.391 \pm 0.003) \text{ cm}^2/\text{V/s}$. Using the high granularity pixel readout, the trans-
22 verse and longitudinal diffusion coefficients were measured to correspond to an
23 effective thermal diffusion temperature of 314 K and 384 K respectively. For
24 429 detected ions, the precision on the absolute drift distance is expected to be
25 1.33 mm for a mean drift distance of 20 mm.

26 *Keywords:* Micromegas, gaseous pixel detector, micro-pattern gaseous
27 detector, Timepix, GridPix, negative ion time projection chamber

28 **1. Introduction**

29 In a negative ion Time Projection Chamber (TPC), ionisation charge is
30 transported to the readout plane by negatively charged ions instead of elec-
31 trons, thereby reducing the diffusion down to the thermal limit [1]. The TPC
32 detects ionisation from interactions in the gas of the TPC. The primary ionisa-
33 tion electrons are captured by the highly electronegative CS₂ gas component,
34 and the ions formed drift to the anode by the electric field. The track position
35 resolution depends on the electron capture length, and the transport properties

*Corresponding author. Telephone: +31 20 592 2000
Email address: c.ligtenb@nikhef.nl (C. Ligtenberg)
Preprint submitted to Elsevier

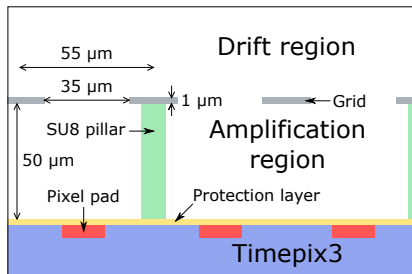


Figure 1: Schematic drawing of the cross-section of a GridPix detector, with some of the components and dimensions indicated.

36 in the gas. In the high field amplification region near the anode, the electrons
 37 detach and an avalanche occurs which is detected by the readout electronics.

38 Negative ion TPCs can be used for directional dark matter searches. For
 39 example, in the Drift IId experiment [2] a negative ion TPC was operated using a
 40 low pressure 30:10 Torr $\text{CF}_4:\text{CS}_2$ gas mixture. It was demonstrated that when
 41 oxygen was present in the gas mixture, extra species of ions called minority
 42 carriers with a larger mobility were created [3]. From the difference in arrival
 43 time of the different ion species at the readout plane, the absolute position in
 44 the drift direction was reconstructed without the need of knowing the event
 45 time in the detector [4].

46 In this paper an exploratory study of GridPix technology to read out a
 47 negative ion TPC is presented. A GridPix consists of a CMOS pixel chip with
 48 integrated amplification grid added by MEMS postprocessing techniques [5, 6].
 49 GridPix detectors based on the Timepix chip were extensively studied as TPC
 50 readouts for a future collider experiment [7] and have been used in the CERN
 51 Axion Solar Telescope [8], see also [9] for an overview of applications. However,
 52 the original Timepix chip has a limited readout rate, and cannot simultaneously
 53 record the time of arrival and the amount of detected charge. This has been
 54 overcome by the next generation GridPix [10] based on the Timepix3 [11] chip.

55 Recently a quad module with four Timepix3 based GridPix chips was devel-
 56 oped for a future collider experiment [12]. The Timepix3 chip can be operated
 57 with a low threshold of $515 e^-$, and has a low equivalent noise charge of about
 58 $70 e^-$. The GridPix TPC readout is sensitive to single charge carriers, and has
 59 a fine granularity of $55 \mu\text{m} \times 55 \mu\text{m}$. Because of this fine granularity and the
 60 low diffusion of ions, a negative ion TPC with GridPix readout can provide an
 61 excellent spatial resolution without a magnetic field. This first investigation
 62 focuses on the operation of the quad module in an already existing setup at
 63 atmospheric pressure.

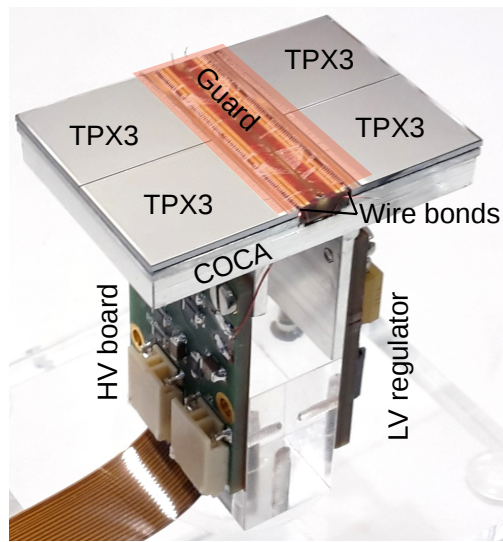


Figure 2: Picture of the quad module with four Timepix3 GridPixes (TPX3) mounted on a cold carrier plate (COCA). The central guard was not yet installed to show the underlying wire bond PCB, and its operating position is indicated with a transparent rectangle. On the right the Low Voltage (LV) regulator is partially hidden behind the aluminium mechanical support, and on the left the High Voltage (HV) board and the flexible Kapton cable are visible. This picture was previously published in [12].

64 2. Quad detector

65 2.1. Gridpix

66 The GridPix is based on the Timepix3 chip [11], which has 256×256 pixels
67 with a pitch of $55 \mu\text{m} \times 55 \mu\text{m}$. On the surface of the chip a $4 \mu\text{m}$ thick silicon-
68 rich silicon nitride resistive protection layer is deposited in order to prevent
69 damage to the readout electronics from discharges of the grid. Silicon-rich silicon
70 nitride is regular silicon nitride (Si_3N_4) doped with extra silicon to make it
71 conductive. On top of the protection layer, $50 \mu\text{m}$ high pillars of the epoxy-
72 based negative photoresist SU8 support a $1 \mu\text{m}$ thick aluminium grid with $35 \mu\text{m}$
73 diameter circular holes aligned to the pixels. Some of the components and
74 dimensions are schematically drawn in Figure 1. The Timepix3 chip can measure
75 a precise Time of Arrival (ToA) using a 640 MHz TDC. In addition for every
76 hit a time over threshold (ToT) is measured, which can be converted into a
77 detected charge by test pulse calibrations. The Timepix3 chip has a data driven
78 readout, and is connected to a speedy pixel detector readout (SPIDR) board at
79 a speed of 160 Mbps [13].

80 2.2. Quad module

81 The quad module shown in Figure 2, consists of four GridPix chips and is
82 optimised for a high fraction of sensitive area of 68.9%. The external dimensions
83 are $39.6 \text{ mm} \times 28.38 \text{ mm}$ and it can be tiled to cover arbitrarily large areas. The
84 four chips which are mounted on a cooled base plate (COCA), are connected
85 with wire bonds to a common central 6 mm wide PCB. A 10 mm wide guard
86 electrode is placed over the wire bonds 1.1 mm above the aluminium grids, in
87 order to prevent field distortions of the electric drift field. The guard is the
88 main inactive area, and its dimensions are set by the space required for the
89 wire bonds. On the back side of the quad module, the PCB is connected to
90 a low voltage regulator. The aluminium grids of the GridPixes are connected
91 by $80 \mu\text{m}$ insulated copper wires to a high voltage (HV) filtering board. The
92 module consumes about 8 W of power of which 2 W is used in the LV regulator.

93 2.3. Experimental setup

94 Eight quad modules were embedded in a box, resulting in a total of 32 chips.
95 A schematic 3-dimensional drawing of the detector is shown in Figure 3. When
96 the measurements were taken, one single quad module with four chips could be
97 read out per SPIDR board. Hardware to simultaneously read out multiple quad
98 modules with one SPIDR board is under development. A schematic drawing
99 of the setup is shown in Figure 4. The internal dimensions of the box are
100 79 mm along the x -axis, 192 mm along the y -axis, and 53 mm along the z -axis
101 (drift direction), and it has a maximum drift length (distance between cathode
102 and readout anode) of 40 mm. The drift field is shaped by a series of parallel
103 CuBe field wires of $50 \mu\text{m}$ diameter with a wire pitch of 2 mm and guard strips
104 are located on all of the four sides of the active area. In addition, six guard
105 wires are suspended over the direct boundaries of the chips, because the chip

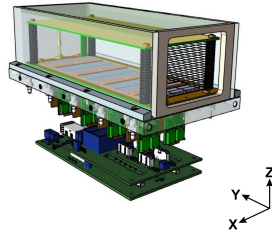


Figure 3: Schematic 3-dimensional render of the 8-quad module detector for illustration purposes.

106 edges are at a ground potential, which would otherwise distort the electric drift
 107 field. The wires are located at a distance of 1.15 mm from the grid planes, and
 108 their potential is set to the potential at this drift distance. The box has one
 109 Kapton window and three optical glass windows (type H-K9L) to facilitate laser
 110 measurements.

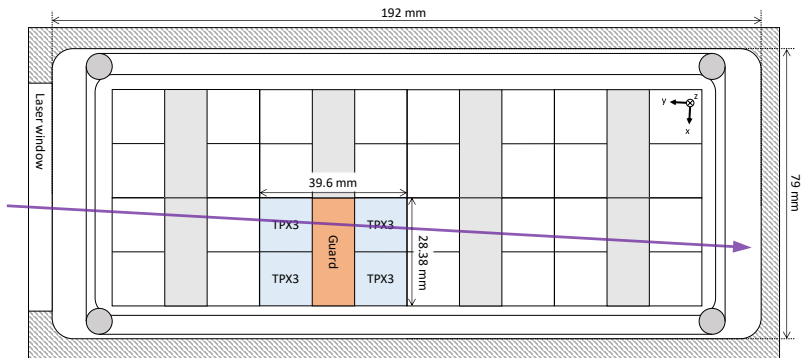


Figure 4: Schematic drawing of the 8-quad module detector with one quad in operation. The laser track direction is shown in purple.

111 The gas volume of 780 ml is continuously flushed with a 93.6/5.0/1.4 gas mix-
 112 ture (by volume) of Ar/iC₄H₁₀/CS₂ at atmospheric pressure. The gas is argon
 113 based, because the setup is also used for research on TPCs with an argon based
 114 gas for future colliders. The isobutane gas was added as a quencher to absorb UV
 115 photons produced in the avalanches, and the CS₂ concentration is chosen high
 116 enough to capture electrons shortly after the ionisation ($\lesssim 200 \mu\text{m}$). A small
 117 amount of oxygen (650 ppm–1150 ppm) and water vapour (about 4000 ppm) are
 118 present in the drift volume because of diffusion and outgassing of some of the
 119 materials. A few ppb of tetra-methyl-phenylene-diamine (TMPD) molecules
 120 are added to enhance laser ionisation in the gas [14]. The TMPD was added
 121 through sublimation by directing the inflowing gas through a tube containing
 122 the solid TMPD grains. Once introduced, a noticeable concentration can remain
 123 in the setup for at least months under normal conditions. During data taking,
 124 the temperature was 297 K and the pressure was 1030 mbar. The experimental
 125 parameters are summarised in Table 1.

126 An amplification field strength $E_{\text{amplification}}$ of 76 kV/cm is achieved in the
 127 50 μm wide gap by setting the grid voltage to -380 V . The pixel pads are
 128 normally at zero potential. A hit is registered if the charge on a pixel pad
 129 is above the threshold set to about $515 e^-$. The mean collected charge of the
 130 selected hits is about $1000 e^-$. The gain is approximately 1000, and the single ion
 131 detection efficiency is expected to be 60%. A higher gain and single ion detection
 132 efficiency can be achieved by increasing the amplification field strength.

133 Tracks of ionisation are created by a pulsed 337 nm N₂ laser at a rate of
 134 2.5 Hz with a pulse duration of 1 ns [14]. This laser is operated using the MOPA
 135 (Master Oscillator Power Amplifier) principle to obtain a beam near the diffrac-
 136 tion limit. The parallel beam can accurately be directed in the gas volume by
 137 means of two remotely controlled stages.

138 Data was taken using the data-driven mode of the Timepix3 chip in a series
 139 of nine automated experimental runs. The time of the laser pulse was added to
 140 the pixel data stream. During a run, the drift field was set to a specific strength
 141 and the beam was positioned at six different drift distances 6 mm apart and at
 142 four different x -positions. Measurements of 2400 laser pulses per run are taken
 143 in a time frame of approximately 17 minutes.

Table 1: Overview of the experimental parameters. The ranges indicate the variation over the total data taking time

Number of runs	9
Run duration	17 minutes
E_{drift}	100 – 500 V/cm
$E_{\text{amplification}}$	76 kV/cm
Threshold	$515 e^-$
Temperature	295.9 – 297.0 K
Pressure	1030 – 1029 mbar
Oxygen concentration	650 – 1150 ppm
Water vapour concentration	$\sim 4000 \text{ ppm}$

144 **3. Analysis**

145 In the analysis the laser position is compared to the reconstructed position
 146 from the quad detector. The laser track is defined by the recorded stage position
 147 as a line parallel to the y -axis. The per pulse variations are smaller than $15\ \mu\text{m}$.
 148 The recorded stage position is taken as the reference to which the four chips
 149 are aligned by rotation in two dimensions, and shifts in the two dimensions
 150 perpendicular to the laser beam. The position of detected ionisation in the
 151 pixel plane is a direct translation from the pixels column (x -direction) and row
 152 number (y -direction). To reduce noise, only hits with a time over threshold
 153 above $0.1\ \mu\text{s}$ are considered. A time over threshold of $0.1\ \mu\text{s}$ corresponds to
 154 a charge close to the threshold of $515\ e^-$. From the known laser pulse time,
 155 the z -position can be calculated as the product of the measured drift time t
 156 and the drift velocity v_{drift} . To remove noise from scattered laser light hitting
 157 the readout directly, hits between $1\ \mu\text{s}$ before and $1\ \mu\text{s}$ after the laser pulse are
 158 removed. All of these cuts are applied in the entire analysis below. To clean
 159 up further the data set for diffusion measurements only, in section 4.3 hits are
 160 required to be within $2\ \text{mm}$ of a laser track in the x -direction and to be within
 161 $5\ \text{mm}$ of the laser track in the z -direction. The alignment and the measurement
 162 of the drift velocity is an iterative process.

163 An example of a resulting drift time spectrum is shown in Figure 5 for the
 164 run at a drift field strength E_{drift} of $300\ \text{V/cm}$. Other experiments using a
 165 $30:10:1$ Torr $\text{CF}_4:\text{CS}_2:\text{O}_2$ gas mixture could distinguish three different minority
 166 carriers as separate peaks in the drift time spectrum [3]. In contrast, in our
 167 measurements only one secondary peak can be found, which is slightly broader
 168 than the primary one. This could be due to e.g. overlapping drift time distribu-
 169 tions, the much lower oxygen concentration, or the much higher water vapour
 170 concentration in our gas mixture affecting the minority carrier(s) production.

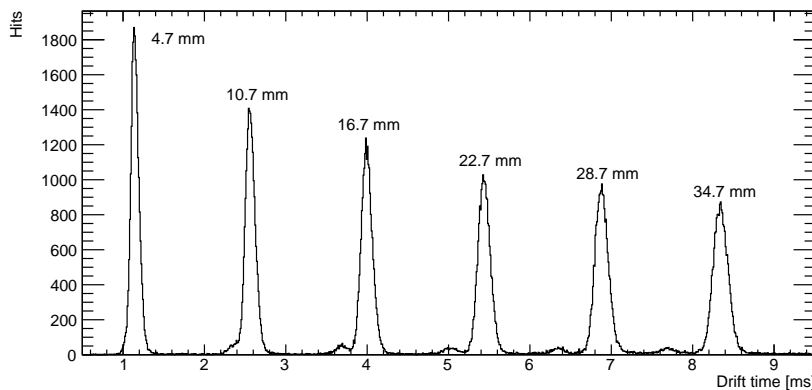


Figure 5: Drift time distribution for 400 laser pulses per z -position, annotated with the drift distance as recorded by the laser stage.

171 In order to determine the drift properties, a ‘global’ fit is made per run.
 172 Each run corresponds to a given electric field strength. A run has measurements
 173 taken at different drift distances. The drift time t distribution is fitted with a
 174 combination of two Gaussian distributions per laser z -position:

$$g(t) = n_{\text{hits}} \left[\frac{f_1}{\sigma_1 \sqrt{2\pi}} \exp\left(-\frac{(t - \mu_1)^2}{2\sigma_1^2}\right) + \frac{f_2}{\sigma_2 \sqrt{2\pi}} \exp\left(-\frac{(t - r_2 \mu_1)^2}{2\sigma_2^2}\right) + \frac{f_{\text{noise}}}{u_{\text{width}}}\right], \quad (1)$$

175 where n_{hits} is the number of hits, u_{width} is the width of a uniform distribution
 176 related to the fitted t range and f_1 is the fraction of the number of detected
 177 ions from majority carrier(s) given by $f_1 = 1 - f_2 - f_{\text{noise}}$. Four parameters are
 178 different for each drift distance, and two parameters are the same for all drift
 179 distances. The mean time μ_1 , the standard deviation of the majority carrier
 180 distribution σ_1 , the standard deviation of the minority carrier(s) distribution
 181 σ_2 and the fraction of the number of ions in the flat noise distribution f_{noise} ,
 182 are fitted per drift distance. In the fit, the fraction of the number of ions from
 183 minority carrier(s) f_2 and the ratio of majority carrier mobility to the minority
 184 carrier(s) mobility r_2 are equal for all drift distances.

185 4. Performance

186 4.1. Number of hits

187 The mean total number of detected hits per laser pulse is 43. The number of
 188 hits can be tuned by adjusting the laser intensity, and the spread on the number
 189 of hits is dominated by per pulse variations of the laser intensity. In this gas, a
 190 minimum ionising particle is expected to create about 100 ionisation pairs per
 191 cm of which about 60 will be detected as hits per cm, because of the 60 % single
 192 ion detection efficiency at a gain of 1000. An example event display showing
 193 the ionisation for a single laser pulse is presented in Figure 6.

194 The GridPix is capable of detecting more than one hit per laser pulse per
 195 pixel. The dead time per pixel for the Timepix3 chip after being hit is the
 196 time over threshold plus 475 ns, so about 1 μ s. With a drift velocity of a few
 197 m/s, even two hits originating from the same position can both be detected,
 198 because they are sufficiently separated due to diffusion. In this case the number
 199 of hits is small, and there is only a small probability of two ions arriving on
 200 the same pixel, but for highly-ionising events the multi-hit capabilities can be
 201 advantageous.

202 4.2. Drift velocity measurements

203 The average drift times for the majority and minority charge carrier(s) are
 204 plotted as a function of the drift distance in Figure 7 for a drift field strength of
 205 300 V/cm. The drift velocity of the minority carrier is found to be 8.1% higher
 206 than that of the majority carrier.

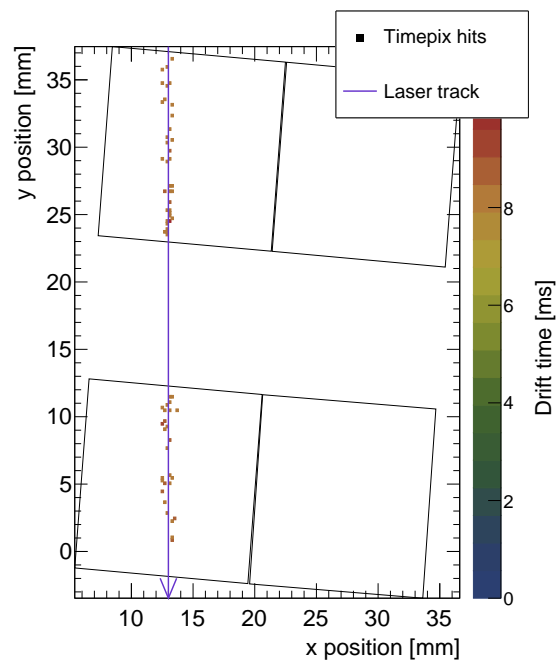


Figure 6: Example of the detected ionisation from one laser pulse with 71 hits in total. The position of the laser track (purple line) and chip edges (black outlines) are drawn in global coordinates. The pixel hits are not to scale.

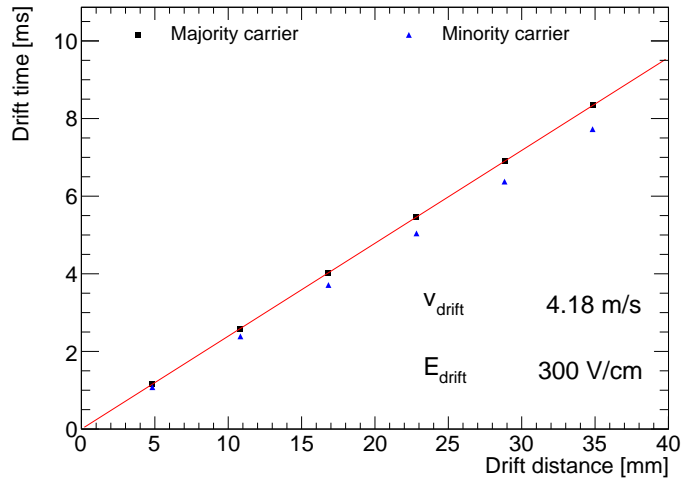


Figure 7: Drift time as a function of the drift distance for the majority and minority carriers. The statistical error is not shown, because it is negligible compared to the systematic uncertainties.

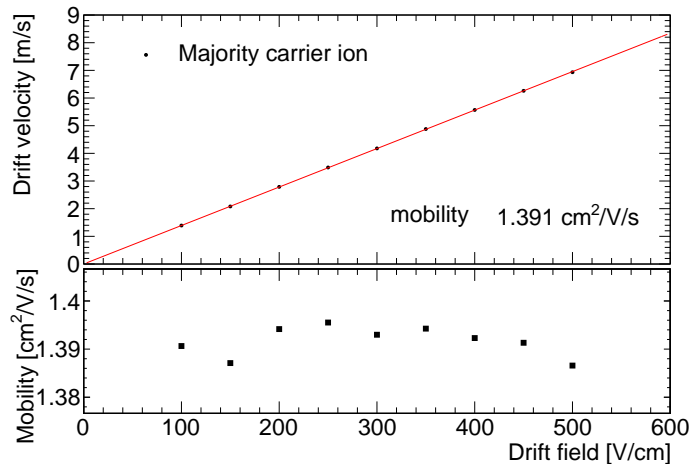


Figure 8: Drift velocity of the majority carrier ion as a function of the drift field. The mobility is acquired from a straight line fit constrained to pass through the origin (0,0). The statistical error is not shown, because it is negligible compared to the systematic uncertainties.

207 The drift velocity measurement is repeated for 9 electric field strengths in
 208 the range 100 V/cm to 500 V/cm. The drift velocity of the majority carrier
 209 v_{drift} as function of the electric field is shown in Figure 8. The mean measured
 210 mobility (defined as the drift velocity divided by the electric field strength) is
 211 $(1.391 \pm 0.003) \text{ cm}^2/\text{V/s}$. The uncertainty of the measured mobility is estimated
 212 as the r.m.s. of the given values, and is probably dominated by fluctuations
 213 in the (local) temperature and gas composition. Because of the unique gas
 214 composition the mobility cannot directly be compared to the results from other
 215 experiments. However, the mobility is the same order of magnitude as previous
 216 measurements. Reference [1] found a mobility of $(1220 \pm 51) \text{ cm}^2/\text{V/s mbar}$ for
 217 a 9:1:14.5 Ar:CH₄:CS₂ gas mixture at a pressure of 40 Torr (53 mbar), which
 218 corresponds to a mobility of $(1.18 \pm 0.04) \text{ cm}^2/\text{V/s}$ at a pressure of 1030 mbar.
 219 Reference [15] found a mobility of $0.71 \text{ cm}^2/\text{V/s}$ in a 200:500 Torr CS₂:He gas
 220 mixture.

221 4.3. Diffusion measurements

222 As the ions drift towards the readout plane, they diffuse which gives them
 223 a Gaussian spread in the longitudinal and transverse direction. The amount of
 224 diffusion is characterised by the standard deviation of the Gaussian distribution
 225 σ_i , where i stands for the longitudinal direction z or the transverse direction x .
 226 This can be expressed as

$$\sigma_i^2 = \sigma_{i0}^2 + D_i^2 z, \quad (2)$$

227 where σ_{i0} is the standard deviation at zero drift, D_i the diffusion coefficient,
 228 and z the drift distance.

229 The standard deviation in the transverse direction σ_x is acquired from a fit of
 230 a Gaussian function to the measured x positions of all detected ions including the
 231 minority carrier(s) ions. In the longitudinal direction the standard deviation σ_z
 232 is acquired from a fit of the sum of two Gaussian functions, which represent the
 233 contribution from the majority carrier ions, and the minority carrier(s) ions, see
 234 Equation (1). The drift time is converted to a distance using the measured drift
 235 velocity of the majority carrier v_{drift} . As an example, the standard deviation
 236 as a function of drift distance for the run at a drift field strength E_{drift} of
 237 300 V/cm is shown in Figure 9. In comparison to the systematic uncertainties,
 238 the statistical error is negligible.

239 The constant contribution in Equation 2 is roughly independent of the elec-
 240 tric field, and on average found to be $\sigma_{x0} = (84 \pm 4) \mu\text{m}$ in the transverse direc-
 241 tion which can predominantly be attributed to the laser beam width plus some
 242 small per laser pulse variation. In the longitudinal direction $\sigma_{z0} = (141 \pm 8) \mu\text{m}$
 243 is measured on average over all runs. This can predominantly be attributed to
 244 the laser beam width plus per laser pulse variations, the spread on the distance
 245 traveled by electrons before they are captured by the CS₂ molecules and possible
 246 unrecognised minority carrier(s).

247 The diffusion coefficient depends on the electric field strength, and the mea-
 248 surements are shown in Figure 10. Because of the much larger systematic un-
 249 certainties, the statistical errors are neglected. At low drift field strengths, the

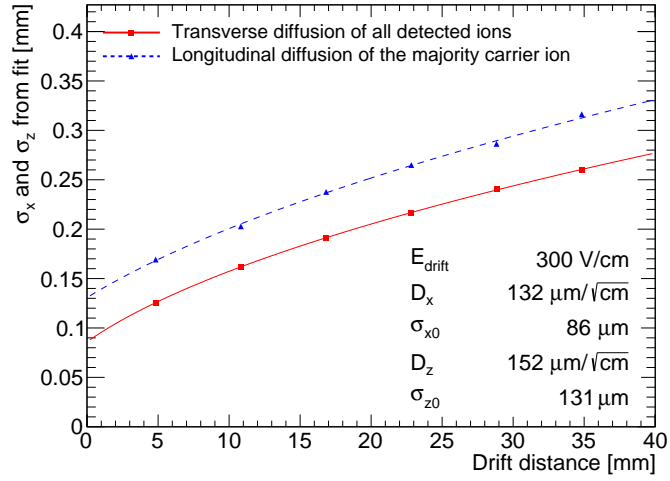


Figure 9: Standard deviation of the hit positions of all detected ions in the transverse direction, and the standard deviation of the hit positions of the majority carrier ions in the longitudinal direction. Both are shown as a function of drift distance for the run with $E_{\text{drift}} = 300 \text{ V/cm}$. The data is fitted with Equation (2).

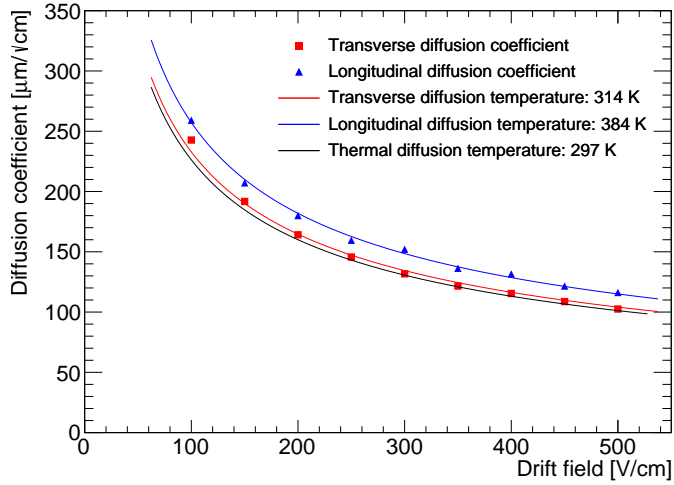


Figure 10: The longitudinal diffusion coefficient of the majority carrier ions, and the transverse diffusion of all detected ions. Both are plotted as a function of drift field E , and fitted with Equation (3). For comparison the expectation for thermal diffusion is shown.

250 ions have thermal energy and the diffusion coefficient can be expressed as

$$D_{\text{thermal}} = \sqrt{\frac{2k_{\text{B}}T}{eE}}, \quad (3)$$

251 where k_{B} is the Boltzmann constant, T is the temperature of the gas, e is the
 252 charge of the ion, and E is the electric field strength (see e.g. [16]). Both the
 253 transverse and longitudinal diffusion coefficients are fitted with Equation (3)
 254 with the temperature T as a free parameter. The transverse diffusion corre-
 255 sponds to an effective temperature of 314 K, which is slightly above the gas
 256 temperature. The effective temperature of the longitudinal diffusion is rather
 257 high, 384 K. This can possibly be explained by unrecognised minority carrier(s).
 258 A simple thermal model with a $1/\sqrt{E_{\text{drift}}}$ dependence describes the data well.

259 In other experiments using a low pressure CS_2 gas, the longitudinal diffusion
 260 is found to be in agreement with the thermal values [17]. In a 500 Torr He and
 261 200 Torr CS_2 gas mixture, longitudinal diffusion coefficients slightly below to
 262 the thermal values are found [15].

263 4.4. Reconstruction of drift distance

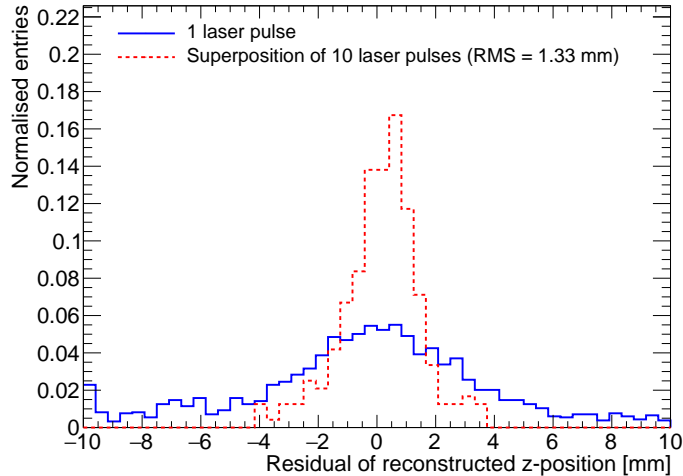


Figure 11: Residual of reconstructed z -position for single laser pulses and a superposition of ten laser pulses for all six drift distances (4.7 mm, 10.7 mm, 16.7 mm, 22.7 mm, 28.7 mm, and 34.7 mm).

264 The difference in drift velocity between the majority carrier and minority
 265 carrier(s) ions can be used to reconstruct the absolute drift distance. Previously,
 266 this technique was demonstrated in a 30:10:1 Torr $\text{CS}_2:\text{CF}_4:\text{O}_2$ gas mixture with
 267 a spread on the reconstructed drift distance of ± 2 cm for a mean drift distance
 268 of about 25 cm [4]. A precision of 16 mm was achieved using a similar technique

269 using an SF₆ gas [18]. Besides the difference in time of arrival between the
270 majority carrier and minority carrier(s), the detected spread due to diffusion
271 can be used to determine the drift distance. A precision of 1 cm was achieved
272 by measuring the transverse spread for 0.8 cm-long alpha track segments in a
273 70:30 He:CO₂ gas mixture at atmospheric pressure [19].

274 Here, fiducialisation is applied to data from the run at the largest drift
275 field of 500 V/cm which gives the best signal peak separation, and also has the
276 highest oxygen concentration of about 1150 ppm. About 4.4% of the hits are
277 attributed to the minority carrier(s), whose mobility is 8.1% higher than that
278 of the majority carrier.

279 The reconstruction proceeds by performing per event a binned maximum
280 likelihood fit of Equation (1) to the measured relative arrival time of ions from
281 one or more laser pulses. A new parameter t_0 is introduced to absorb the
282 now unknown laser pulse time. The parameters f_2 , r_2 , f_{noise} are fixed to their
283 previously fitted values. For σ_1 Equation (2) is used, and σ_2 is by approximation
284 fixed to σ_1 . The parameter μ_1 (the mean arrival time of the primary carrier
285 peak) are acquired from the fit. The z -position is calculated using the measured
286 drift velocity v_{drift} . The detected spread in the transverse direction is not utilised
287 in the determination of the z -position.

288 By comparing the reconstructed z -position to the z -position of the laser
289 stage for all six drift distances (4.7 mm, 10.7 mm, 16.7 mm, 22.7 mm, 28.7 mm,
290 and 34.7 mm), the residual shown in Figure 11 is obtained. There are 2401 laser
291 pulses with a mean number of 43 detected ions and 240 superpositions of ten
292 laser pulses with a total mean number of 429 ions. From a single laser pulse, on
293 average 43 ions are detected and 76 % of the laser pulses fall within the ± 10 mm
294 range. The determined z -position has a rather large spread, because very few
295 minority carrier(s) ions are detected. In order to estimate the performance for a
296 larger number of ions, a superposition of ten laser pulses at the same z -position
297 is made by shifting their arrival times by the time difference between the laser
298 pulses. From this we acquire emulated pulses with a mean total number of 429
299 detected ions of which about 19 ions are attributed to the minority carrier(s).
300 The resulting r.m.s. is 1.33 mm for 239 out of the 240 combined laser pulses for
301 a mean drift distance of 20 mm. For one entry the reconstructed z -position is
302 off by 14 mm, and the r.m.s. is 1.62 mm if it is included as well.

303 5. Conclusions and outlook

304 The performance of a GridPix detector to readout a negative ion TPC was
305 studied using a quad module with four Timepix3 based GridPix chips. The TPC
306 is operated using a 93.6/5.0/1.4 gas mixture (by volume) of Ar/iC₄H₁₀/CS₂
307 with a small amount of oxygen and water vapour at a pressure of 1030 mbar
308 and a temperature of 297 K. Tracks were produced by a pulsed N₂ laser. The
309 1.56 ns time resolution of the Timepix3 chips allows for a precise determination
310 of the drift properties in the longitudinal direction. The measured ion mobility
311 for the majority carrier ions is $(1.391 \pm 0.003) \text{ cm}^2/\text{V/s}$. Using the high granu-
312 larity pixel readout, the transverse and longitudinal diffusion coefficients were

313 measured to correspond to an effective thermal diffusion temperature of 314 K
314 and 384 K respectively. A simple thermal model with a $1/\sqrt{E_{\text{drift}}}$ dependence
315 describes the data well. This confirms the expected low diffusion coefficient for
316 ions. Furthermore, the GridPix has an efficiency of approximately 60% to detect
317 single drift ions. This can be improved by operating the device at a higher gain.
318 By using also the relative arrival time of 429 detected ions with a mean drift
319 distance of 20 mm, the absolute z -position can be measured with an expected
320 precision of 1.33 mm.

321 In the future, a GridPix TPC readout might be of interest to directional
322 dark matter experiments. The often desired operation at low pressure can be
323 investigated in combination with a GridPix readout. For these experiments gas
324 mixtures containing SF₆ have some advantages [17], and can also be studied for
325 operation with a GridPix readout. Alternatively, for operation around atmo-
326 spheric pressure replacing argon with the lighter helium could increase nuclear
327 recoils lengths important for directional dark matter searches[1, 20].

328 All in all, the fine granularity and high timing precision of the GridPix TPC
329 readout in combination with the capability to detect single ions, provide an
330 excellent position resolution in the longitudinal and transverse direction.

331 Acknowledgements

332 This research was funded by the Netherlands Organisation for Scientific Re-
333 search NWO. The authors want to acknowledge the support of the mechanical
334 and electronics departments at Nikhef.

335 References

- 336 [1] C. Martoff, D. Snowden-Ifft, T. Ohnuki, N. Spooner, M. Lehner, Suppress-
337 ing drift chamber diffusion without magnetic field, Nucl. Instrum. Meth. A
338 440 (2000) 355–359. doi:10.1016/S0168-9002(99)00955-9.
- 339 [2] J. Battat, et al., Low Threshold Results and Limits from the DRIFT
340 Directional Dark Matter Detector, Astropart. Phys. 91 (2017) 65–74.
341 arXiv:1701.00171, doi:10.1016/j.astropartphys.2017.03.007.
- 342 [3] D. P. Snowden-Ifft, Discovery of Multiple, Ionization-Created Anions in
343 Gas Mixtures Containing CS₂ and O₂ (8 2013). arXiv:1308.0354.
- 344 [4] J. Battat, et al., First background-free limit from a directional dark matter
345 experiment: results from a fully fiducialised DRIFT detector, Phys. Dark
346 Univ. 9-10 (2015) 1–7. arXiv:1410.7821, doi:10.1016/j.dark.2015.06.
347 001.
- 348 [5] P. Colas, A. P. Colijn, A. Fornaini, Y. Giomataris, H. van der Graaf,
349 E. H. M. Heijne, X. Llopart, J. Schmitz, J. Timmermans, J. L. Vissch-
350 ers, The readout of a GEM- or micromegas-equipped TPC by means of the
351 Medipix2 CMOS sensor as direct anode, Nucl. Instrum. Meth. A535 (2004)
352 506–510. doi:10.1016/j.nima.2004.07.180.

- 353 [6] M. Campbell, M. Chefdeville, P. Colas, A. P. Colijn, A. Fornaini,
354 Y. Giomataris, H. van der Graaf, E. H. M. Heijne, P. Kluit, X. Llopart-
355 Cudie, J. Schmitz, J. Timmermans, J. L. Visschers, Detection of single elec-
356 trons by means of a micromegas-covered MediPix2 pixel CMOS readout cir-
357 cuit, Nucl. Instrum. Meth. A540 (2005) 295–304. [arXiv:physics/0409048](https://arxiv.org/abs/physics/0409048),
358 [doi:10.1016/j.nima.2004.11.036](https://doi.org/10.1016/j.nima.2004.11.036).
- 359 [7] M. Lupberger, Y. Bilevych, H. Blank, D. Danilov, K. Desch, A. Hamann,
360 J. Kaminski, W. Ockenfels, J. Tomtschak, S. Zigann-Wack, Toward the
361 Pixel-TPC: Construction and Operation of a Large Area GridPix Detector,
362 IEEE Trans. Nucl. Sci. 64 (5) (2017) 1159–1167. [doi:10.1109/TNS.2017.](https://doi.org/10.1109/TNS.2017.2689244)
363 [2689244](https://doi.org/10.1109/TNS.2017.2689244).
- 364 [8] C. Krieger, J. Kaminski, M. Lupberger, K. Desch, A GridPix-based X-ray
365 detector for the CAST experiment, Nucl. Instrum. Meth. A 867 (2017)
366 101–107. [doi:10.1016/j.nima.2017.04.007](https://doi.org/10.1016/j.nima.2017.04.007).
- 367 [9] J. Kaminski, Y. Bilevych, K. Desch, C. Krieger, M. Lupberger, GridPix de-
368 tectors – introduction and applications, Nucl. Instrum. Meth. A 845 (2017)
369 233–235. [doi:10.1016/j.nima.2016.05.134](https://doi.org/10.1016/j.nima.2016.05.134).
- 370 [10] C. Ligtenberg, et al., Performance of a GridPix detector based on the
371 Timepix3 chip, Nucl. Instrum. Meth. A 908 (2018) 18–23. [arXiv:1808.](https://arxiv.org/abs/1808.04565)
372 [04565](https://doi.org/10.1016/j.nima.2018.08.012), [doi:10.1016/j.nima.2018.08.012](https://doi.org/10.1016/j.nima.2018.08.012).
- 373 [11] T. Poikela, J. Plosila, T. Westerlund, M. Campbell, M. De Gaspari,
374 X. Llopart, V. Gromov, R. Kluit, M. van Beuzekom, F. Zappone,
375 V. Zivkovic, C. Brezina, K. Desch, Y. Fu, A. Kruth, Timepix3: a 65K
376 channel hybrid pixel readout chip with simultaneous ToA/ToT and sparse
377 readout, JINST 9 (05) (2014) C05013.
378 URL <http://stacks.iop.org/1748-0221/9/i=05/a=C05013>
- 379 [12] C. Ligtenberg, et al., Performance of the GridPix detector quad, Nucl.
380 Instrum. Meth. A 956 (2020) 163331. [arXiv:2001.01540](https://arxiv.org/abs/2001.01540), [doi:10.1016/](https://doi.org/10.1016/j.nima.2019.163331)
381 [j.nima.2019.163331](https://doi.org/10.1016/j.nima.2019.163331).
- 382 [13] B. van der Heijden, J. Visser, M. van Beuzekom, H. Boterenbrood, S. Kulis,
383 B. Munneke, F. Schreuder, SPIDR, a general-purpose readout system for
384 pixel ASICs, JINST 12 (02) (2017) C02040. [doi:10.1088/1748-0221/12/](https://doi.org/10.1088/1748-0221/12/02/C02040)
385 [02/C02040](https://doi.org/10.1088/1748-0221/12/02/C02040).
- 386 [14] F. Hartjes, A diffraction limited nitrogen laser for detector calibration in
387 high energy physics, Ph.D. thesis, University of Amsterdam (1990).
388 URL [https://www.nikhef.nl/pub/services/biblio/theses_pdf/](https://www.nikhef.nl/pub/services/biblio/theses_pdf/thesis_F_Hartjes.pdf)
389 [thesis_F_Hartjes.pdf](https://www.nikhef.nl/pub/services/biblio/theses_pdf/thesis_F_Hartjes.pdf)
- 390 [15] C. Martoff, R. Ayad, M. Katz-Hyman, G. Bonvicini, A. Schreiner, Negative
391 ion drift and diffusion in a TPC near 1 bar, Nucl. Instrum. Meth. A 555
392 (2005) 55–58. [arXiv:physics/0406114](https://arxiv.org/abs/physics/0406114), [doi:10.1016/j.nima.2005.08.](https://doi.org/10.1016/j.nima.2005.08.103)
393 [103](https://doi.org/10.1016/j.nima.2005.08.103).

- 394 [16] W. Blum, L. Rolandi, W. Riegler, Particle detection with drift cham-
395 bers, Particle Acceleration and Detection, Springer, 2008. doi:10.1007/
396 978-3-540-76684-1.
397 URL <https://www.springer.com/gp/book/9783540766834>
- 398 [17] N. Phan, R. Lafler, R. Lauer, E. Lee, D. Loomba, J. Matthews, E. Miller,
399 The novel properties of SF₆ for directional dark matter experiments, JINST
400 12 (02) (2017) P02012. arXiv:1609.05249, doi:10.1088/1748-0221/12/
401 02/P02012.
- 402 [18] T. Ikeda, T. Shimada, H. Ishiura, K. Nakamura, T. Nakamura, K. Miuchi,
403 Development of a Negative Ion Micro TPC Detector with SF₆ Gas for the
404 Directional Dark Matter Search (4 2020). arXiv:2004.09706.
- 405 [19] P. Lewis, S. Vahsen, I. Seong, M. Hedges, I. Jaegle, T. Thorpe, Absolute
406 Position Measurement in a Gas Time Projection Chamber via Transverse
407 Diffusion of Drift Charge, Nucl. Instrum. Meth. A 789 (2015) 81–85. arXiv:
408 1410.1131, doi:10.1016/j.nima.2015.03.024.
- 409 [20] E. Baracchini, G. Cavoto, G. Mazzitelli, F. Murtas, F. Renga, S. Tomassini,
410 Negative Ion Time Projection Chamber operation with SF₆ at nearly at-
411 mospheric pressure, JINST 13 (04) (2018) P04022. arXiv:1710.01994,
412 doi:10.1088/1748-0221/13/04/P04022.